Drying paths of phase-separating solution coatings exposed to humidity

Masato Yamamura
Department of Applied Chemistry, Kyushu Institute of Technology,
Sensui 1-1, Tobata, Kitakyushu, Fukuoka 804-8550, Japan

Abstract

Drying process paths, i.e., time-dependent trajectories of solution compositions on a phase diagram, were examined for coatings of a water-immiscible acrylic monomer dissolved in ethanol and exposed to humidity. The absorption of water vapor quenched the solution into a thermodynamic non-equilibrium state and promoted a spontaneous phase separation when the water content in the solution exceeded a critical value. A simultaneous mass-loss and heat-flux measurement technique was proposed and adapted for phase-separating coatings to determine the evaporation rates of two volatile components with different latent heats of vaporization. The measured drying paths agreed with those predicted from a drying model that takes into account the gas-diffusion-limited evaporation and composition-dependent activities. The numerical predictions also revealed that the pseudo-azeotrope determined the critical drying conditions, under which any drying paths on the phase diagram did not cross the two-phase region, and thus the drying solutions remained stable.

Keywords: drying process path, phase separation, pseudo-azeotrope, heat flux, numerical simulation

Introduction

Reactive acrylic monomers are widely used in the coating industry to fabricate protective [1, 2], antireflective [3], antifogging [4], antibacterial [5], and self-healing [6] thin film products coated over large areas. In photo-curing thin film processing, the monomer is dissolved in a solvent with a photo-initiator, coated on a moving solid substrate, dried in unsaturated air, and subsequently exposed to an ultraviolet (UV) light. The photo-initiator molecules absorb the light to generate free radicals, which attack the monomers to trigger polymerization reactions that solidify the film.

The fate of the drying monomer solution film depends on the thermodynamic stability of the system. A homogeneous film forms when the solution is stable. By contrast, the solution containing a water-immiscible monomer becomes unstable when water vapor is absorbed into the drying solution to increase the water concentration above a certain threshold. The inherent incompatibility between the monomer and water promotes a spontaneous phase separation between water-rich and

monomer-rich phases, leading to uneven surface topographies and changing the optical properties of the UV-cured coating products. To manipulate the desirable microstructures in thin liquid monomer films, it is important to predict the time-dependent trajectories of the average or local compositions on the phase diagram, which are occasionally referred to as drying process paths [7].

Figure 1 shows a schematic phase diagram of a monomer-solvent-water ternary mixture. The binodal curve divides the diagram into two regions, i.e., a stable one-phase region and an unstable or metastable two-phase region. The solid curve represents the drying path when the solvent preferentially evaporates in humid air. The water concentration initially increases not only because of the solvent evaporation that concentrates the mixture but also the water absorption driven by the difference in partial pressure between the liquid surface and the air. The drying path crosses the binodal curve at a particular location on the phase diagram and enters the two-phase region, resulting in an onset of a phase separation. The water content then decreases as the solvent and water evaporate simultaneously.

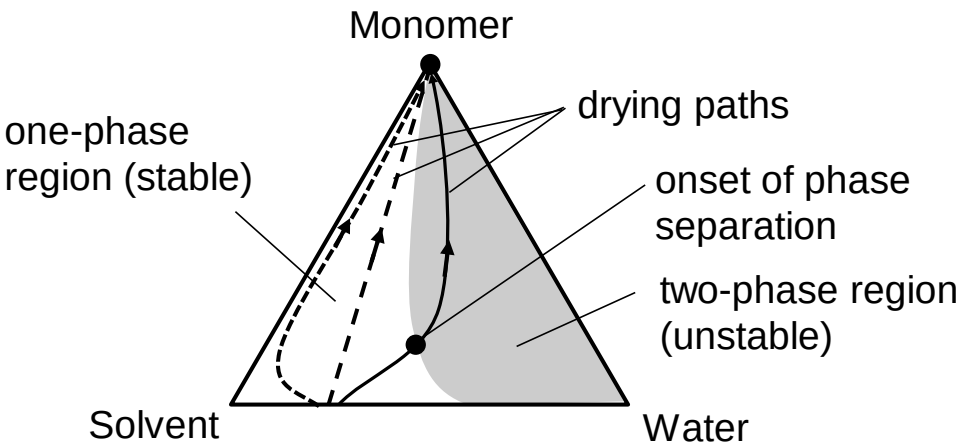

Fig. 1 Schematic ternary phase diagram and drying process paths in a monomer-solvent-water system. A binodal curve divides the diagram into a stable one-phase region (white) and a two-phase region (dark). The solid curve represents a drying path when the solvent preferentially evaporates while water absorption proceeds from humid air to the solution. The drying path crosses the binodal curve at a location (closed circle) on the phase diagram and enters the two-phase region, resulting in an onset of the phase separation. Dashed curves show the drying paths at different initial compositions.

According to previous theoretical studies, drying paths in non-ideal mixtures often exhibit complex branches and/or bifurcations with unstable/stable nodes [8]. A small compositional change at the branch alters the directions of the drying paths, and thereby determines which solvent selectively evaporates, whereas the other components increase their concentrations in the mixture. The selectivity depends upon the diffusive resistance in the liquid film [9] as well as the velocity, temperature, and solvent concentration in the drying air [10, 11]. Under particular drying conditions, the drying process becomes non-selective, i.e., the mass ratio of the two solvents maintains a constant value during the course of evaporation, which is often referred to as a dynamic azeotropes or pseudo-azeotrope [12–14]. The pseudo-azeotrope differs from the thermodynamic azeotrope because it is determined by not only the thermodynamic equilibrium at the air–liquid interface but also by the mass transfers in the liquid and gas phases.

However, experimental validation of the theoretical prediction has been limited to thermodynamically stable systems of solvent mixtures [8, 9] and polymer-solvent-water miscible solutions [15]. Notwithstanding extensive studies on numerical predictions of drying paths in phase-separating non-equilibrium systems [7, 16–20], to the best of our knowledge, few attempts have been made to quantitatively compare predicted and measured drying process paths. The major difficulty in the quantitative validation of immiscible or partially miscible thin film coatings stems from the fact that (i) reliable data are lacking for the vapor pressures and diffusion coefficients as functions of the temperature and concentration in a non-equilibrium state, and (ii) phase-separated domain structures sometimes hamper high-precision optical measurements to determine the time evolutions in the compositions. In the former, spontaneous phase separation emerges in a non-equilibrium solution film. The diffusion coefficients in the system locally vary in each separating phase, which grows with time to form three-dimensional microstructures with different compositions. Since the local compositions would change as the phase evolve, the composition-dependent diffusion coefficients become a complex function of drying time, making the exact evaluation of the diffusion coefficients difficult without achieving high measurement resolutions both in time and space.

From the experimental viewpoints, optical measurement techniques are occasionally useless for phase-separating coatings because the optical signals are readily scattered by the microstructures that evolve inside the liquid. Despite the recent progress made in time-resolved monitoring of compositions using Raman [21–24] and infrared [25] spectroscopies, *in-situ* measurements of drying paths for phase-separated opaque films remain a challenge.

In this study, we proposed a novel measurement technique to directly determine the drying paths of phase-separating monomer-ethanol-water ternary systems by combining a heat flux [26] with simultaneous mass-loss measurements. We showed a quantitative agreement between the

measurements and predictions based on a gas-diffusion-limited drying model. We also addressed the role of a pseudo-azeotrope in drying paths of the phase-separating ternary solution coatings.

Experimental

We used Dipentaerythritol-Hexaacrylate ($C_{28}H_{34}O_{13}$, DPHA, Shin-Nakamura Chemical Co., Ltd.) with six acryloyl groups as an acrylic liquid monomer and ethanol (Fujifilm Wako Pure Chemical Co. Ltd.) as the solvent, respectively. DPHA shows good solubility in ethanol but poor solubility in water. The materials were used as received without further purification. DPHA was dissolved in ethanol to prepare solutions with different initial compositions. UV-Vis spectroscopy (MultiSpec-1500, Shimadzu) revealed that the solution transmittance at a wavelength of 400 nm significantly decreased with increasing water concentration above a certain critical content, that is, the cloud point, at which the solution became opaque owing to the onset of a phase separation. The measured cloud points in equilibrium were collected to depict the binodal curve, that is, the border between the one-phase and two-phase regions on the ternary phase diagram.

The solution was coated on a 1.1-mm thick glass substrate with an initial film thickness of 500 microns. The coated area was specified as 36 cm^2 by gluing an aluminum shim on the substrate. The sample solution with the pre-determined volume was ejected from a micro-pipette and coated onto the specified area. The solutions spread over the substrate surface without applying any external forces. The mean initial thickness (h_0) was obtained from the liquid volume (V) divided by the liquid surface area (S) as $h_0 = V/S$. A conductive plate heater (Kitazato MP-10DMH) was used to maintain a constant temperature of the substrate ranging between 25 ºC and 55 ºC. No forced flow of air was imposed in the drying chamber although a natural convection could occur on the heated substrate. The coating was then mounted on an electronic balance (Sartorius, MSE2203S) to measure the decrease in film mass at a sampling rate of 1 Hz. When the coating contains two different volatile components, that is, ethanol and water, the mass loss measurement enables us to determine the "total" evaporation rates only. To separate the drying rates of the two solvents, we combined the mass loss and heat flux measurements. Consider a solution coating containing solvent components A and B. The total drying rate (r_{total}) is given as the sum of the drying rate of each solvent, i.e.,

$$r_{total}(t) = r_A(t) + r_B(t). \qquad (1)$$

where r_A and r_B denote the drying rates of components A and B, respectively. Assuming a steady heat transfer across the coating, the heat flux in the drying liquid is expressed as the sum of the latent heat and the convection heat transfer in the gas phase as

$$q(t) = h_{air}^{G}(T_i(t) - T_b) + r_A(t)\Delta H_A + r_B(t)\Delta H_B. \qquad (2)$$

where T_i is the film surface temperature, T_b is the temperature of bulk air, h^G_{air} is the heat transfer coefficient, and ΔH_i is the latent heat of solvent i (where i = A, B). Combining Eqs. (1) and (2) gives the expression for the drying rate of solvent A as:

$$r_A = \frac{1}{\Delta H_A - \Delta H_B}\{q(t) - h^G_{air}(T_i(t) - T_b) - r_{total}(t)\Delta H_B\}. \qquad (3)$$

We obtain a similar expression for the drying rate of solvent B by simply replacing the subscript A with B in Eq. (3). Thus, we can determine the drying rate of each solvent from simultaneous measurements of q(t) and r_{total}(t) as a function of the drying time. In addition, integrating the drying rates r_A and r_B with time enabled us to calculate the average residual solvent amounts at different drying times, and hence, the drying path as a trajectory of the time-evolving composition on the phase diagram. It is worth noting that the heat-flux method proposed here does not require optical transparency of the samples nor temperature uniformity across the coating.

To measure the heat flux, we used a 0.4-mm thick circular heat-flux sensor (Captec, HF-D40) with a diameter of 40 mm. The sensor consisted of thermocouple arrays and gave a voltage proportional to the heat flux across the thickness with a sensitivity of 35.3 μV/(W·m^2). The sensor was adhered to the bottom surface of the substrate using a 0.5-mm thick conductive adhesive film (Kitagawa Industries Co. Ltd, CPVS-0.5F) with a thermal conductivity of 2.0 W/(m·K). To ensure one-dimensional heat conduction in the thickness direction, the sensor was surrounded by a 90 mm × 90 mm panel with the same thermal conductivity and the thickness as those of the sensor. The measured voltage increased as the evaporation began, maintained an almost constant value for a certain drying time, and then decreased as the evaporation rate decreased. To minimize the external disturbances in the mass-loss measurement, the output voltage from the sensor was stored in a wireless data logger (Hioki E. E. Co., Ltd., 3671) directly mounted on the electronic balance, converted into digital signals, and transferred to a wireless receiver (Hioki E. E. Co., Ltd., 3913) connected to a computer. The validity of the heat-flux measurement has been proven by comparing the drying rates measured by the gravimetric and heat-flux methods for pure solvent coatings, as shown elsewhere [26].

To determine the surface temperature of the drying liquid film (T_i), we used a steady-state solution of unidirectional heat conduction across the thickness, expressed as a function of the heat flux (q) and the temperature of the sensor (T_S) as follows:

$$T_i(t) = T_S(t) - \left(\frac{h(t)}{\lambda} + \frac{h_g}{\lambda_g} + \frac{h_f}{\lambda_f} + K\right)q(t). \qquad (4)$$

where h and λ represent the thickness and thermal conductivity of the drying solution, respectively. The thermal resistances in the liquid layer (h/λ) were comparable to those in the glass substrate (h_g/λ_g), and the conductive film (h_f/λ_f), where h_g and λ_g denote the thickness and thermal conductivity of the substrate, respectively, and h_f and λ_f denote the thickness and thermal conductivity of the adhesive film, respectively. We also considered the thermal resistance (K) owing to the existence of a thin layer of air, which was trapped between the sensor−adhesive and the glass−adhesive interfaces. To determine the K value, we conducted a preliminary heat conduction experiment without casting a liquid and measured the surface temperature of the substrate (T_g), the sensor temperature, and the heat flux. By omitting the liquid conduction term, h/λ, and replacing T_i with the measured surface temperature in Eq. (4), we obtained a good linear relationship between the temperature difference $\Delta T (= T_S - T_g)$ and the heat flux, q, and obtained a constant $K = 2.4 \times 10^{-3}$ m$^2 \cdot$K/W from the slope of the $\Delta T - q$ plot.

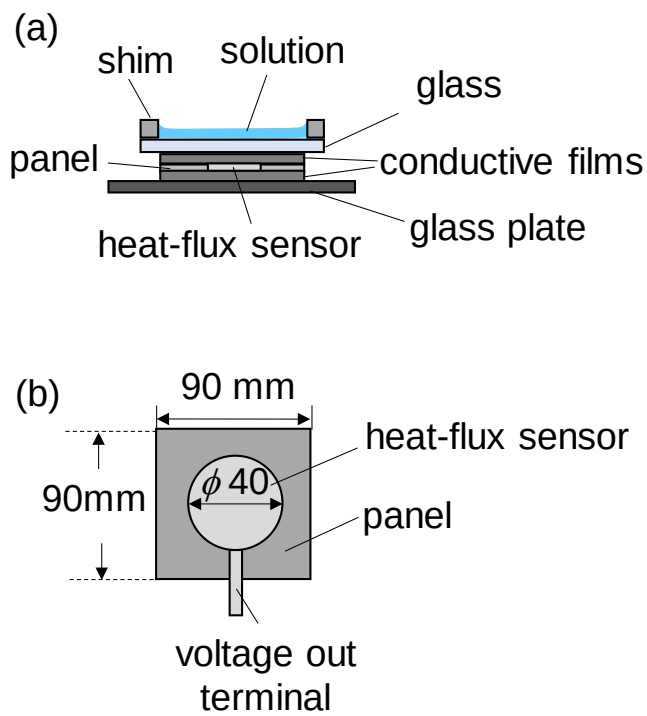

Figure 2 Heat flux sensor setup: (a) cross-sectional view (b) top view

Modeling

We theoretically predicted the drying process paths of drying monomer-ethanol coatings exposed to humid air or an unsaturated ethanol vapor. Consider an isothermal liquid film coated on an impermeable substrate with a uniform thickness, the model of which is based on the following assumptions: (1) the drying is gas-diffusion limited, i.e., the convective resistance to mass transfer

of the gas phase is much greater than the diffusive resistance in the liquid layer, (2) the axial diffusion is negligible, (3) the composition profiles are uniform across the thickness, (4) the mass transfer coefficients in the gas phase are constant, and (5) the evolutions of phase-separated structures have a negligible influence on the evaporation rates. The mass transfer coefficients were given by k_w = 6.29×10^{-3} m/s for water and $k_e = 3.60 \times 10^{-3}$ m/s for ethanol, respectively, where k_w was determined by a direct comparison between the measured and predicted drying rates of the water layer at a given temperature. To estimate k_e, we used the relationship $k_e/k_w = (D_{e\text{-air}}/D_{w\text{-air}})^n$ where $D_{e\text{-air}}$ and $D_{w\text{-air}}$ are mutual diffusion coefficients in ethanol–air and water–air gas mixtures. The exponent n = 3/4 was given by the expression of the heat transfer coefficient for a national convection on a heated plate [27] and the analogy between heat and mass transfers. Note that we simply assumed that the dynamics of solvent evaporation in phase-separating solutions are the same as those in thermodynamically stable solutions, as has been applied in the literature [16, 28], although some previous studies have shown that the evolutions of the phase-separated microstructures retarded [29] or enhanced [30, 31] the solvent evaporation during the falling-rate period, where the internal diffusive resistance in the liquid becomes rate-limiting. We assumed a gas-diffusion-limited drying for the sake of simplicity in the present modeling and thereby neglected the effects of phase separation on the drying kinetics.

We solved the one-dimensional mass balance equation for the volatile component j as:

$$\frac{dm_j}{dt} = -\frac{k_j M_j}{RT} A(a_j P^*_{i,j} - P_{b,j}) \qquad (5).$$

where m_j is the mass of component j in the solution, t is the drying time, R is the gas constant, T is the coating temperature, A is the coating surface area, and a_j is the activity of component j. In addition, $P^*_{i,j}$ and $P_{b,j}$ are the saturated vapor pressure of pure component j at the air–liquid interface and the partial vapor pressure of component j in bulk air, respectively. The equations for water ($j = w$) and ethanol ($j = e$) were discretized over time using the finite difference method. To examine the effect of gas loading, we defined the degree of gas saturation of component j as $S_j = P_{b,j} / P^*_j$, where P^*_j denotes the saturated vapor pressure of the solvent at a given gas temperature of interest. The degree of saturation of the water vapor is identical to the relative humidity based on the definition.

To predict the activities of volatile components as a function of compositions, we used the UNIversal Functional-group Activity Coefficient (UNIFAC) group contribution model, in which the properties of each building block or functional group of the components were considered [32]. The group parameters of the UNIFAC model were taken from [33]. For instance, the model parameters for DPHA were obtained by considering CH_2O, CH_2COO, C=C, C, and CH_2 groups. The activity coefficient of the j-th component, γ_j, is written in combinatorial (γ_j^C) and residual (γ_j^R) parts as

to $\ln\gamma_j = \ln\gamma_j^C + \ln\gamma_j^R$. Each part was calculated by considering the segment surface area and volume contributions, the number of the segment on each molecule, and the surface and volume fraction of each component in the mixture.

Results and discussion

Figure 3 shows a comparison between the measured (open circles) and predicted (closed triangles) drying paths at the initial solvent content of 3 g-ethanol/g-DPHA and the gas saturation of water at $S_w = 0.86$. The temperature of the drying air was equal to the initial coating temperature and was fixed at 25 °C. The average compositions at different drying times were plotted on the phase diagram every 80 s. The initial ethanol-DPHA solution was thermodynamically stable. The monomer concentration monotonically increased as the film shrank due to ethanol evaporation. When the solution dried in humid air, the partial vapor pressure of water in the air ($P_{b,j}$) was higher than that at the evaporating surface ($P^*_{i,j}$), thereby providing a driving force for vapor absorption into the solution film. As the drying path entered the two-phase region, the solution became thermodynamically unstable and spontaneously separated into monomer- and water-rich phases. With a further increase in the average concentration of water, the vapor pressure at the evaporating surface increased and eventually overcame that in air as $P^*_{i,j} > P_{b,j}$, indicating an absorption-evaporation transition above a certain concentration threshold. The evaporation of ethanol then completed and that of water followed, leaving the monomer film with a certain amount of residual water. A comparison between the locations of the measured and predicted drying paths showed a good agreement, indicating the validity of the present modeling. The theory underestimated the water concentration in the late drying stages, possibly because we neglected the internal diffusion resistance and concentration gradients across the film. We here note that the solution film locally ruptured under particular drying conditions. However, our preliminary experiments showed that the liquid film ruptured only when the initial solvent content exceeded the critical values of 10 g-solvent/g-DPHA, which was much higher than the present solvent content of 3 g-solvent/g-DPHA, indicating that the film rupture was not the reason for the discrepancy between the measured and predicted drying process paths. It is also worth noting that we obtained the averaged compositions in the two-phase region, although the local compositions differed in each separating phase. A supplemental photo-curing experiment using bis(2,4,6-trimethylbenzoyl)phenyl-phosphine oxide as a photo-responsive additive showed that interconnected phase-separated structures developed on the coating surface when the UV light source of 365 nm in wavelength and 20 mW/cm^2 in intensity was irradiated onto the surface just after completion of the drying process (not shown here).

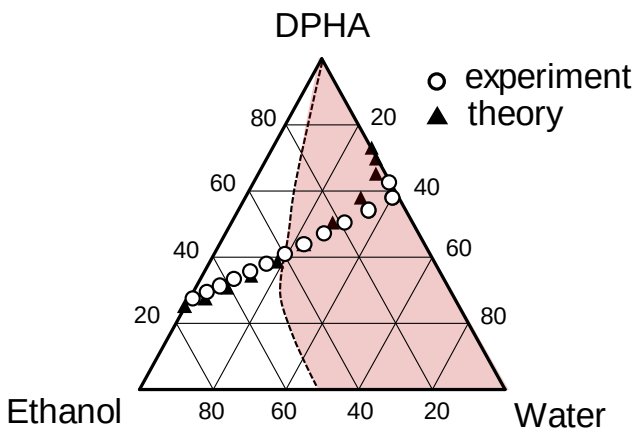

Figure 3 A comparison between measured (open circles) and predicted (closed triangles) drying paths at the initial solvent content of 3 g-ethanol/g-DPHA, the vapor saturation of water of S_w = 0.86, and the air temperature of 25 °C. The average compositions at different drying times were plotted on the phase diagram for every 80 s. The dashed curve in the phase diagram shows the binodal curve that splits the one-phase (white) and two-phase (dark colored) regions. The measured path matched the theoretical predictions, except in the late drying stage where the theory underestimated the water concentration.

It is of practical importance to predict the drying conditions, under which the liquid remains stable and no phase separation emerges in the course of evaporation. To examine this, we systematically predicted the drying paths at different initial solution compositions, gas saturations, and drying temperatures. Figure 4 shows the variations in the drying process paths for (a) dry air (S_w = S_e =0), (b) mildly humid air (S_w = 0.5, S_e = 0), (c) humid air fully saturated by water vapor (S_w = 1.0, S_e = 0), and (d) dry air partially saturated with ethanol vapor (S_w = 0, S_e = 0.5). We assumed constant temperatures of drying air and a solution of 25 ºC and 55 ºC, respectively. The initial mass fraction of DPHA was fixed at 0.01. The predicted process paths exhibited a particular branch during the early evaporation stages, i.e., water preferentially evaporated at a high initial concentration of ethanol (path A), whereas ethanol preferentially dried to concentrate the water when the initial ethanol concentrations were lower than a critical value (paths C and D). The drying became non-selective in the intermediate case (path B), indicating the existence of a pseudo-azeotrope. The hatched area in the figure denotes the regime, in which the collected drying paths do not cross the two-phase region. Path A was retained inside this area throughout the drying process, and thus the coating remained thermodynamically stable. By contrast, paths C and D in the non-hatched area

entered the two-phase region at certain drying times. The border between the hatched and unhatched areas was expressed as a straight line upon which the ethanol-water mass ratio remained constant and thus agreed with the pseudo-azeotrope line [9]. The pseudo-azeotrope line also matched the tangent of the binodal curve, indicating that no phase separation would take place on the drying paths that are located on the left side of the pseudo-azeotrope line, regardless of how we choose the initial compositions. These facts imply that the pseudo-azeotrope provides a useful guide to choose proper drying paths to keep the monomer coatings stable. To the best of our knowledge, such a role of a pseudo-azeotrope for coatings dried in a non-equilibrium state has not been previously reported.

The numerical predictions also revealed that the drying behavior was sensitive to gas saturation in air. An increase in water saturation led to the disappearance of the pseudo-azeotrope and shrank the hatched region in size, as shown in Figs. 4b and 4c. In the case of drying in fully saturated water vapor (i.e., S_w = 1.0), phase separation can be prevented only in narrow regions at high DPHA concentrations because the drying would complete before the water concentration reached the critical value for the onset of phase separation. On the contrary, the "no-phase-separation" region expanded when ethanol vapor was loaded in the drying air (Fig. 4d). The slower ethanol evaporation at higher ethanol vapor concentration led to a shift of the pseudo-azeotrope line toward lower ethanol contents and made the solutions less prone to a phase separation. Furthermore, a new branch appears between the drying paths P and Q on the phase diagram. When the initial water concentration exceeded a threshold, the absorption of ethanol vapor into the solution took place, resulting in an increase in the ethanol concentration during the early evaporation stages (path Q) as in path A (see Fig. 4a). We here emphasize that the locations of the border between the hatched and unhatched regions depend on drying kinetics. In Figure 4b, the border is expressed as the path E, which first curves as the liquid absorbs water vapor in the early evaporation stages but then extends as a straight line on the phase diagram in the intermediate drying stages, keeping the concentration of water constant. This is because the increasing rate of water concentration via the vapor absorption and the ethanol evaporation balances with the decreasing rate of the water concentration via its evaporation. We obtained the same trend in the path H in Figure 4c. In the alternative case when we have a pseudo-azeotrope, the border agrees with the pseudo-azeotrope lines (path B in Figure 4a and path M in Figure 4d).

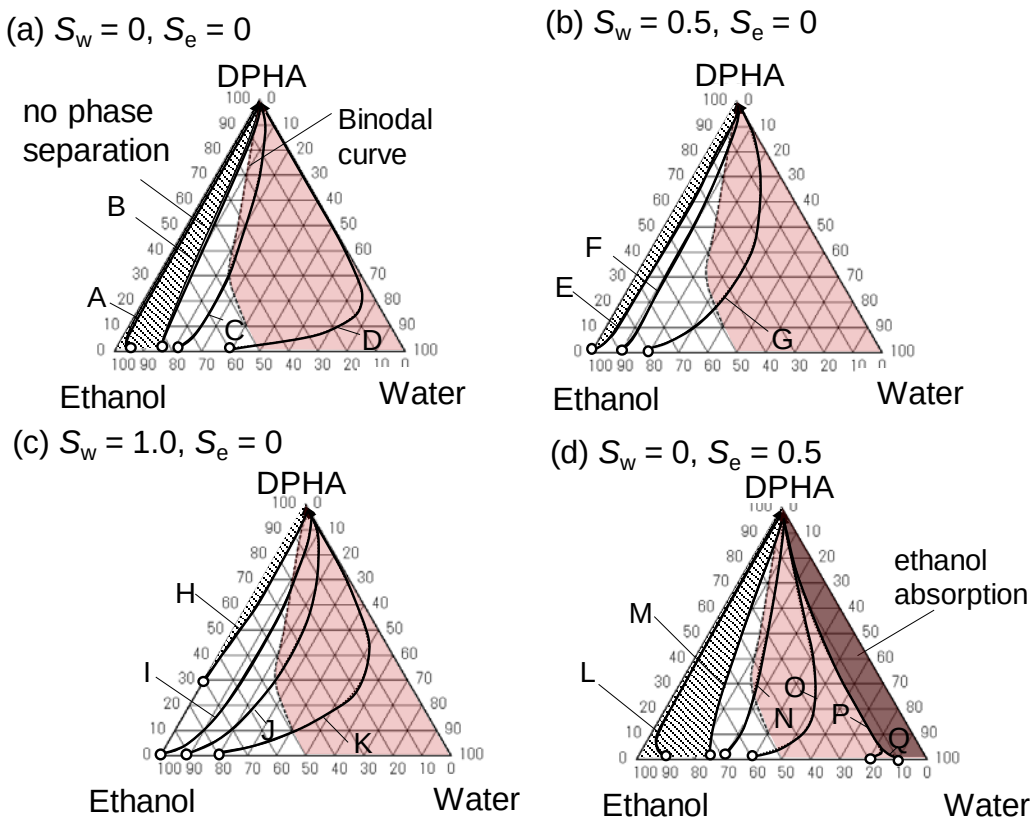

Fig. 4 Variations in drying process paths at different degrees of vapor saturations. The colored area represents the two-phase region where the solutions become thermodynamically metastable or unstable. The hatched area denotes the characteristic no-phase separation regime where the collected drying paths do not cross the two-phase region. The initial mass fractions are (A) w_e = 0.95, w_w = 0.04, (B) w_e = 0.83, w_w = 0.16, (C) w_e = 0.78, w_w = 0.21, (D, O) w_e = 0.60, w_w = 0.39, (E, I) w_e = 0.99, w_w = 0, (F, J, L) w_e = 0.90, w_w = 0.09, (G, K) w_e = 0.80, w_w = 0.19, (H) w_e = 0.70, w_w = 0, (M) w_e = 0.75, w_w = 0.24, (N) w_e = 0.70, w_w = 0.29, (P) w_e = 0.20, w_w = 0.79, and (P) w_e = 0.10, w_w = 0.89, where w_e and w_w denote the mass fractions of ethanol and water, respectively. We assumed constant temperatures of 25 °C in drying air and 55 °C in the solution. The mass transfer coefficients were 6.29×10^{-3} m/s for water and 3.60×10^{-3} m/s for ethanol.

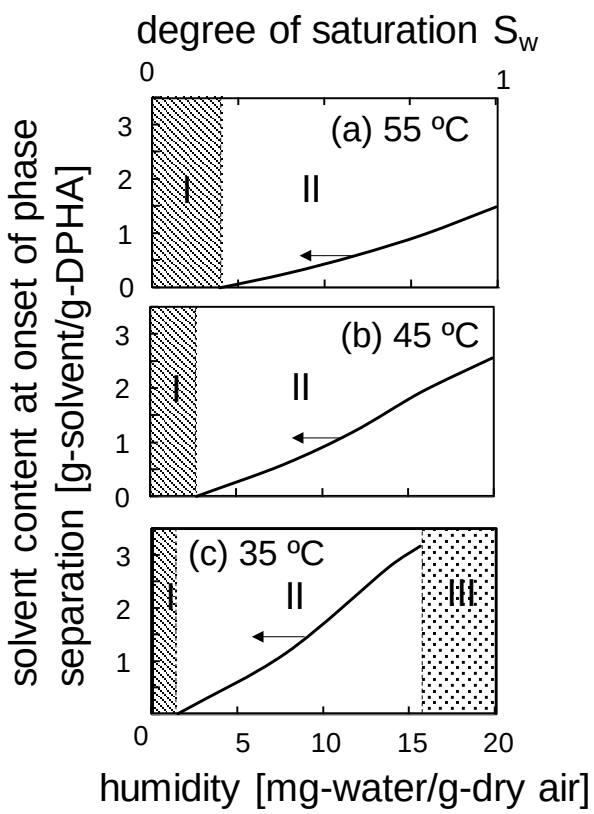

Fig. 5 Drying operation maps at different solution temperatures of (a) 55 °C, (b) 45 °C, and (c) 35 °C. The map is divided into three regions of (I) no phase separation, (II) phase separation, and (III) vapor condensation during the course of ethanol evaporation. The initial mass fractions of ethanol and water are $w_e = 0.909$ and $w_w = 0$, respectively. The temperature and ethanol saturation in drying air are 25 °C and $S_e = 0$.

To further explore the critical drying conditions, we summarized the drying operation maps in Fig. 5 at different liquid temperatures of (a) 55 °C, (b) 45 °C, and (c) 35 °C. The solid curves in the figure represent the critical solvent-to-monomer mass ratios at the onset of phase separation, which were determined by the local compositions at the intersection points of the binodal curve and the predicted drying paths on the phase diagram. The initial mass fractions of ethanol and water were fixed at $w_e = 0.909$ and $w_w = 0$, respectively, and the temperature in drying air was 25 °C

As illustrated in Fig. 5a, the solutions remained stable at low air humidity below a critical value (regime I), but phase separated at higher humidity as the water vapor in the air was absorbed into the drying solution (regime II). The critical solvent content monotonically increased with increasing humidity, indicating that the phase separation began at shorter drying times. With a decrease in drying temperature, the phase-separation regime II expanded toward a lower humidity and the critical

solvent content increased at a given humidity (Fig. 5b). These facts can be understood by considering a decrease in the saturated vapor pressure of water at the evaporation surface. The difference in water vapor pressures between the bulk air and the liquid surface increased and drove more vapor to absorb into the drying solution, giving rise to trigger the absorption-induced phase separation at higher solvent contents. In addition, the slower evaporation rates of ethanol at lower temperatures promoted vapor absorption for longer drying times, thereby making the solution less stable. With a further decrease in drying temperature, the surface temperature of the coating became lower than the dew point of the drying air. This would promote the condensation of water vapor onto the evaporating surface under high humidity conditions, as depicted in the dark regime III shown in Fig. 5c. From a practical perspective, the water condensation onto a solution surface may trigger a phase separation as well as drying defects such as surface-tension-driven non-uniformities, dimples [34], and breath figures [35, 36]. Indeed, we observed a surface-tension-driven Marangoni convection in the early drying stages, particularly under high humidity conditions. Although the three-dimensional convection in the liquid can create periodic surface topographies as well as the compositional heterogeneities along the evaporating surface, the convection ceased at a certain drying time because of the increasing viscosity of the solution and the decreasing thickness, both of which tend to increase viscous forces that resist the liquid motion. Examining the effect of the flow instability on the drying process path is interesting but beyond the scope of this present modeling.

We emphasize that the prediction of the drying process paths enables us to shed light on the rich physics of the drying behavior of monomer solution coatings. The preferential evaporation of water and ethanol is tunable by changing either the initial solution composition or the gas saturation of the solvents in the drying air, as shown in Fig. 4. The pseudo-azeotrope line divides the composition regions where drying of either solvent becomes preferential. When the pseudo-azeotrope line matches a tangent of the binodal curve, i.e., the composition families for the onset of a phase separation, the line determines the border of the non-phase-separation region where any drying paths in that area do not cross the two-phase region, and thus the drying can proceed without a phase separation. A new branch in the drying process paths appears on the phase diagram when we increase the vapor saturation of ethanol in drying air, leading to a drying regime where the phase separation and the absorption of ethanol vapor can simultaneously emerge during the course of evaporation (Fig. 4d). An increase in the drying temperature was found to expand the operable drying conditions to avoid a phase separation, as illustrated in Fig. 5. These facts provide a practical basis toward a fundamental understanding of how the drying solution coatings accompany the absorption of water vapor and subsequent vapor-induced phase separation and how we can determine the drying conditions to control the microstructure development in the solution films. Although the present

model assumes an isothermal coating with a uniform concentration profile across the thickness and thus predicts only the "average" compositions, an extension of the model into non-isothermal coatings that involve a time-evolution of the concentration gradients in the thickness direction is straightforward by solving coupled diffusion equations [7, 16, 17] and is an area for future studies.

Conclusions

We examined the drying behavior of the solution coatings consisting of a water-immiscible acrylic monomer and ethanol exposed to humid air. The solution absorbed water vapor in the course of evaporation and promoted a spontaneous vapor-induced phase separation when the water content in the solution exceeded a critical value. To determine the drying process paths, we newly proposed a simultaneous mass-loss and heat-flux measurement technique, which enables us to determine the evaporation rates of two volatile components with different latent heats of vaporization. We showed that this technique is applicable to phase-separating opaque coatings and thus overcomes the measurement difficulties in most conventional optical methods. The measured drying paths were compared with the isothermal drying model and showed good agreement with the model predictions. The numerical predictions also revealed the critical drying conditions under which no drying paths on the phase diagram crossed the two-phase region. The predicted pseudo-azeotrope line divided the composition regions where the drying of either solvent became preferential and thus provided a useful guide to keep the drying solutions stable.

Acknowledgement

The author wishes to thank Hirokazu Ohya and Mitsuru Shoji for their technical assistance with the experiments. The author acknowledges the financial support of the Japan Society for the Promotion of Science (JSPS) KAKENHI (20H02507) Grant-in-Aid for Scientific Research B.

References

[1] Lee, JY, Yi, MS, Jeong, HC, Kim, JT, Nam, JH., Noh, SM, Jung, HW, "Characterization of clearcoats containing phosphoric acid-functionalized acrylic polyols for automotive precoated metal sheet coatings." Journal of Coatings Technology and Research, 11, 697-710 (2014).

[2] Li, T, Zhang, P, Chen, B, Liu, S, Deng, J, "Synthesis and properties of UV-curable waterborne urethane modified acrylic coatings with varying vinyl content." Journal of Applied Polymer Science, 137, 49384 (2020).

[3] Yu, YY, Chen, PK, “Nanocomposites of polymer and inorganic nanoparticles prepared by focused microwave polymerization for optical thin films applications.” Thin Solid Films, 544, 48-53 (2013).

[4] Yao, B, Zhao, H, Wang, L, Liu, Zheng, YC, Li, H, Sun, C, “Synthesis of acrylate-based UV/thermal dual-cure coatings for antifogging.” Journal of Coatings Technology and Research, 15, 149-158 (2018).

[5] Degli Esposti, M, Pilati, F, Bondi, M, de Niederhäusern, S, Iseppi, R, Toselli, M, “Preparation, characterization, and antibacterial activity of photocured thymol-doped acrylic resins.” Journal of Coatings Technology and Research, 10, 371-379 (2013).

[6] Wang, S, Wu, Y, Dai, J, Teng, N, Peng, Y, Cao, L, Liu, X, “Making organic coatings greener: Renewable resource, solvent-free synthesis, UV curing and repairability.” European Polymer Journal, 123, 109439 (2020).

[7] Dabral, M, Francis, LF, Scriven, LE, “Drying process paths of ternary polymer solution coating.” AIChE Journal, 48, 25-37 (2002).

[8] Dillon, P, Cronin, K, Byrne, EP, “Evaporation maps for non-ideal ternary mixtures.” Chemical Engineering Science, 126, 641-659 (2015).

[9] Riede, T, Schlünder, EU, “Selective evaporation of a ternary mixture containing one nonvolatile component with regard to drying processes.” Chemical Engineering and Processing, 28, 151-163 (1990).

[10] Viduarre, M, Martinez, J, “Continuous drying of a solid wetted with ternary mixtures.” AIChE Journal, 43, 681-692 (1997).

[11] Martinez, J, Setterwall, F, “Gas-phase controlled convective drying of solids wetted with multicomponent mixtures.” Chemical Engineering Science 9, 2235-2252 (1991).

[12] Thurner, F, Schlünder, EU, “Progress towards understanding the drying of porous materials wetted with binary mixtures.” Chemical Engineering and Processing, 20, 9-25 (1989).

[13] Huang, YS, Sundmacher, K, Qi, Z, Schlünder, EU, “Residue curve maps of reactive membrane separation.” Chemical Engineering Science, 59, 2863-2879 (2004).

[14] Scheepers, F, Stähler, A, Stähler, M, Carmo, M, Lehnert, W, Stolten, D, “Steering and in situ monitoring of drying phenomena during film fabrication.” Journal of Coatings Technology and Research, 16, 1213-1221 (2019).

[15] Putranto, A, Chen, XD, “Drying of a system of multiple solvents: Modeling by the reaction engineering approach.” AIChE Journal, 62, 2144-2215 (2016).

[16] Shojaie, SS, Krantz, WB, Greenberg, AR, “Dense polymer film and membrane formation via the dry-cast process part I. Model development.” Journal of Membrane Science, 94, 255-280 (1994).

[17] Altinkaya, SA, Ozbas, B, “Modeling of asymmetric membrane formation by dry-casting method.” Journal of Membrane Science, 230, 71-89 (2004).

[18] Prakash, SS, Francis, LF, Scriven, LE, “Microstructure evolution in dry cast cellulose acetate membranes by cryo-SEM.” Journal of Membrane Science, 283, 328-338 (2006).

[19] Kuo, CY, Su, SL, Tsai, HA, Wang, DM, Lai, JY, “Formation and evolution of a bicontinuous structure of PMMA membrane during wet immersion process.” Journal of Membrane Science, 315, 187-194 (2008).

[20] Pervin, R, Ghosh, P, Basavaraj, MG, “Tailoring pore distribution in polymer films via evaporation induced phase separation.” RSC Advances, 9, 15593-15605 (2019).

[21] Raupp, SM, Kitz, PG, Siebel, DK, Wunsch, A, Merklein, L, Scharfer, P, Schabel, W, “Modeling of interdiffusion in poly(vinyl acetate)–poly(methyl methacrylate)–toluene multicomponent systems.” Journal of Applied Polymer Science, 136, 47092 (2019).

[22] Yoshihara, H, Yamamura, M, “Concentration profiles in phase-separating photocuring coatings.” Journal of Coatings Technology and Research, 16, 1629-1636 (2019).

[23] Gracia-Medrano-Bravo, VA, Gröne, J, Baesch, S, Scharfer, P, Schabel, W, “Influence of particle shape on the drying regime maps for platelike particle-polymer composites.” Langmuir, 36, 6245-6253 (2020).

[24] Gracia-Medrano-Bravo, VA, Merklein, L, Oberle, N, Batora, M, Scharfer, P, Schabel, W, “Determination of binary interaction parameters for ternary polymer-polymer-solvent systems using Raman spectroscopy.” Advanced Materials Technologies, 2000149 (2020)

[25] Tchakalova, V, Zemb, T, Benczédi, D, “Evaporation triggered self-assembly in aqueous fragrance-ethanol mixtures and its impact on fragrance performance.” Colloids and Surfaces A: Physicochemical and Engineering Aspects, 460, 414-421 (2014).

[26] Yamamura, M, Ohara, K, Mawatari, Y, Kage, H, “Measuring the drying rate of liquid film coatings using heat flux method.” Drying Technology, 27, 817-820 (2009).

[27] Fishenden M, Saunders, OA, Introduction to Heat Transfer 180, Clarendon Press, Oxford (1980).

[28] Matsuyama, H, Teramoto, M, Uesaka, T, “Membrane formation and structure development by dry-cast process.” Journal of Membrane Science, 135, 271-288 (1997).

[29] Yamamura, M, Horiuchi, K, Kajiwara, T, Adachi, K, “Decrease in solvent evaporation rate due to phase separation in polymer films.” AIChE Journal, 48, 2711-2714 (2002).

[30] Yamamura, M, Yamakawa, T, Nasu, T, Orihashi, K, Mawatari, Y, Kage, H, "Effects of polymer end groups on the drying rates of phase separating coatings." Chemical Engineering and Processing: Process Intensification, 68, 55-59 (2013).

[31] Yamamura, M, Yoshihara, H, Mawatari, Y, Kage, H, "Enhanced solvent drying of liquid film coatings by fluorine-base polymeric surfactant addition." Journal of Chemical Engineering of Japan, 45, 441-443 (2012).

[32] Fredenslund, A, Jones, RL, Prausnitz, JM, "Group-contribution estimation of activity coefficients in nonideal liquid mixtures." AIChE Journal, 21, 1086-1099 (1975).

[33] Fredenslund, A, Gmehling, J, Rasmussen, P, "Vapor-liquid equilibria using UNIFAC a group-contribution method" Elsevier (1977).

[34] Yamamura, M, Eikai, S, Mawatari, Y, Kage, H, "Drying-induced hierarchical dimple patterns on partially miscible polymeric films under ordered convections." Drying Technology, 31, 1212-1218 (2013).

[35] Widawski, G, Rawiso, M, François, B, "Self-organized honeycomb morphology of star-polymer polystyrene films." Nature, 369, 387-389 (1994).

[36] Aynard, A, Pessoni, L, Billon, L. "Directed self-assembly in "breath figure" templating of block copolymers followed by soft hydrolysis-condensation: One step towards synthetic bio-inspired silica diatoms exoskeleton." Polymer, 210, 123047 (2020).

List of Figures

Figure 1 Schematic ternary phase diagram and drying process paths in a monomer-solvent-water system. A binodal curve divides the diagram into a stable one-phase region (white) and a two-phase region (dark). The solid curve represents a drying path when the solvent preferentially evaporates while water absorption proceeds from humid air to the solution. The drying path crosses the binodal curve at a location (closed circle) on the phase diagram and enters the two-phase region, resulting in an onset of the phase separation. Dashed curves show the drying paths at different initial compositions.

Figure 2 Heat flux sensor setup: (a) cross-sectional view (b) top view

Figure 3 A comparison between measured (open circles) and predicted (closed triangles) drying paths at the initial solvent content of 3 g-ethanol/g-DPHA, the vapor saturation of water of S_w = 0.86, and the air temperature of 25 °C. The average compositions at different drying times were plotted on the phase diagram for every 80 s. The dashed curve in the phase diagram shows the binodal curve that splits the one-phase (white) and two-phase (dark colored)

regions. The measured path matched the theoretical predictions, except in the late drying stage where the theory underestimated the water concentration.

Fig. 4 Variations in drying process paths at different degrees of vapor saturations. The colored area represents the two-phase region where the solutions become thermodynamically metastable or unstable. The hatched area denotes the characteristic no-phase separation regime where the collected drying paths do not cross the two-phase region. The initial mass fractions are (A) $w_e = 0.95$, $w_w = 0.04$, (B) $w_e = 0.83$, $w_w = 0.16$, (C) $w_e = 0.78$, $w_w = 0.21$, (D, O) $w_e = 0.60$, $w_w = 0.39$, (E, I) $w_e = 0.99$, $w_w = 0$, (F, J, L) $w_e = 0.90$, $w_w = 0.09$, (G, K) $w_e = 0.80$, $w_w = 0.19$, (H) $w_e = 0.70$, $w_w = 0$, (M) $w_e = 0.75$, $w_w = 0.24$, (N) $w_e = 0.70$, $w_w = 0.29$, (P) $w_e = 0.20$, $w_w = 0.79$, and (P) $w_e = 0.10$, $w_w = 0.89$, where w_e and w_w denote the mass fractions of ethanol and water, respectively. We assumed constant temperatures of 25 °C in drying air and 55 °C in the solution. The mass transfer coefficients were 6.29×10^{-3} m/s for water and 3.60×10^{-3} m/s for ethanol.

Fig. 5 Drying operation maps at different solution temperatures of (a) 55 °C, (b) 45 °C, and (c) 35 °C. The map is divided into three regions of (I) no phase separation, (II) phase separation, and (III) vapor condensation during the course of ethanol evaporation. The initial mass fractions of ethanol and water are $w_e = 0.909$ and $w_w = 0$, respectively. The temperature and ethanol saturation in drying air are 25 °C and $S_e = 0$.

Supporting Information

Fig. S1 Variations in the (a) solvent mass and (b) heat flux of evaporating monomer thin film with drying time. The initial ethanol content and the surface temperature of the substrate were 10 g-EtOH/g-DPHA, and 26.0 °C, respectively. The vapor saturation of water was $S_w = 0.49$. The solvent mass decreased almost linearly with time in early evaporation stages, i.e., in a constant-rate period. The measured heat flux maintained an almost constant value for a certain drying time and then decreased as the evaporation rate decreased. The slope of the dashed line represents the initial evaporation rate.